A&A 526, A136 (2011)
DOI: 10.1051/0004-6361/201015020

Astronomy & Astrophysics

The hot horizontal-branch stars in ω Centauri*

S. Moehler[1], S. Dreizler[2], T. Lanz[3], G. Bono[4,5], A. V. Sweigart[6], A. Calamida[1,5], and M. Nonino[7]

[1] European Southern Observatory, Karl-Schwarzschild-Str. 2, 85748 Garching, Germany
e-mail: smoehler,acalamid@eso.org
[2] Georg-August-Universität, Institut für Astrophysik, Friedrich-Hund-Platz 1, 37077 Göttingen, Germany
e-mail: dreizler@astro.physik.uni-goettingen.de
[3] Department of Astronomy, University of Maryland, College Park, MD 20742-2421, USA
e-mail: lanz@astro.umd.edu
[4] Dipartimento di Fisica, Universitá di Roma Tor Vergata, via della Ricerca Scientifica 1, 00133 Roma, Italy
e-mail: bono@roma2.infn.it
[5] INAF - Rome Astronomical Observatory, via Frascati 33, 00040 Monte Porzio Catone, Italy
[6] NASA Goddard Space Flight Center, Code 667, Greenbelt, MD 20771, USA
e-mail: Allen.V.Sweigart@nasa.gov
[7] INAF - Trieste Astronomical Observatory, via G.B. Tiepolo 11, 40131 Trieste, Italy
e-mail: nonino@ts.astro.it

Received 19 May 2010 / Accepted 28 August 2010

ABSTRACT

Context. UV observations of some massive globular clusters have revealed a significant population of stars hotter and fainter than the hot end of the horizontal branch (HB), the so-called blue hook stars. This feature might be explained either by the late hot flasher scenario where stars experience the helium flash while on the white dwarf cooling curve or by the progeny of the helium-enriched sub-population postulated to exist in some clusters. Previous spectroscopic analyses of blue hook stars in ω Cen and NGC 2808 support the late hot flasher scenario, but the stars contain much less helium than expected and the predicted C and N enrichment cannot be verified.

Aims. We compare the observed effective temperatures, surface gravities, helium abundances, and carbon line strengths (where detectable) of our targets stars with the predictions of the two aforementioned scenarios.

Methods. Moderately high resolution spectra of hot HB stars in the globular cluster ω Cen were analysed for radial velocity variations, atmospheric parameters, and abundances using LTE and non-LTE model atmospheres.

Results. We find no evidence of close binaries among our target stars. All stars below 30 000 K are helium-poor and very similar to HB stars observed in that temperature range in other globular clusters. In the temperature range 30 000 K to 50 000 K, we find that 28% of our stars are helium-poor ($\log \frac{n_{\rm He}}{n_{\rm H}} < -1.6$), while 72% have roughly solar or super-solar helium abundance ($\log \frac{n_{\rm He}}{n_{\rm H}} \geq -1.5$). We also find that carbon enrichment is strongly correlated with helium enrichment, with a maximum carbon enrichment of 3% by mass.

Conclusions. A strong carbon enrichment in tandem with helium enrichment is predicted by the late hot flasher scenario, but not by the helium-enrichment scenario. We conclude that the helium-rich HB stars in ω Cen cannot be explained solely by the helium-enrichment scenario invoked to explain the blue main sequence.

Key words. stars: horizontal-branch – stars: evolution – techniques: spectroscopic – globular clusters: individual: NGC 5139

1. Introduction

UV-visual colour–magnitude diagrams of the two very massive globular clusters, ω Cen and NGC 2808, display a rather puzzling "hook-like" feature at the hot end of their extended horizontal branches with stars lying below the canonical horizontal branch (Whitney et al. 1998; D'Cruz et al. 2000; Brown et al. 2001). Similar features were observed in NGC 2419 (Ripepi et al. 2007), NGC 6273 (Piotto et al. 1999), NGC 6715 (Rosenberg et al. 2004), and NGC 6388 (and possibly NGC 6441, Busso et al. 2007). These blue-hook stars cannot be explained within the framework of canonical stellar evolution. Brown et al. (2001) proposed a "flash-mixing" scenario to explain the blue hook stars. According to this scenario, stars that lose an unusually large amount of mass will leave the red giant branch (RGB) before the helium flash and will move quickly to the (helium-core) white dwarf cooling curve before igniting helium (Castellani & Castellani 1993; D'Cruz et al. 1996; Brown et al. 2001). However, the evolution of these "late hot helium flashers" differs dramatically from the evolution of stars that undergo the helium flash on the RGB. When a star flashes at the tip of the RGB or shortly thereafter, the large entropy barrier of its strong hydrogen-burning shell usually prevents the products of helium burning from being mixed to the surface. These canonical stars will evolve to the zero-age horizontal branch (ZAHB) without any change in their hydrogen-rich envelope composition. In contrast, stars that ignite helium on the white dwarf cooling curve, where the hydrogen-burning shell is much weaker, will undergo extensive mixing between the helium- and carbon-rich core and the hydrogen envelope (Sweigart 1997; Brown et al. 2001; Cassisi et al. 2003, 2009;

* Based on observations with the ESO Very Large Telescope at Paranal Observatory, Chile (proposal IDs 075.D-0280(A) and 077.D-0021(A)).

Miller Bertolami et al. 2008). Depending on where the helium flash occurs along the white dwarf cooling curve, the envelope hydrogen will be mixed either deeply into the core ("deep mixing") or only within a convective shell in the outer part of the core ("shallow mixing"). In the case of deep mixing, virtually all of the envelope hydrogen is burned, while in shallow mixing some of the envelope hydrogen remains after the mixing phase (Lanz et al. 2004). One of the most robust predictions of the flash-mixing scenario is an increase in the surface abundance of carbon to 3–5% (deep mixing) or 1% (shallow mixing) by mass. This increase is set by the carbon production during the helium flash and is nearly independent of the stellar parameters.

For these reasons, the flash convection zone will have a composition of about 4% carbon and 96% helium (plus the minor heavier elements) as it grows outward through the core toward the hydrogen shell. Since there is initially no hydrogen in the core, none of this 3α carbon is burned to nitrogen via CNO burning at this stage of the flash. This situation changes, however, once the flash convection zone penetrates into the hydrogen shell, and hydrogen is mixed into the core. This hydrogen will burn on the ^{12}C in the flash convection zone around the point where the mixing timescale is comparable to the timescale of the ^{12}C+proton reaction. If the number of protons is smaller than or of the order of the number of ^{12}C nuclei, the primary outcome of this hydrogen burning is the production of ^{13}C. If, however, there are of the order of two protons for each ^{12}C nuclei, then the ^{12}C can react to produce some ^{14}N. How much ^{14}N is produced will depend on the details of the mixing process. It appears, however, that the primary outcome of this hydrogen burning is the production of ^{13}C with only a much smaller amount of ^{14}N. Thus the predicted surface abundance by mass following flash mixing should be approximately 96% helium, 4% carbon, and possibly a small amount of nitrogen. For both deep and shallow mixing, the blue hook stars should be helium-rich relative to the canonical extreme HB (EHB) stars.

On the other hand, some authors propose that the blue hook stars are the canonical progeny of the helium-rich subpopulation ($Y \approx 0.4$, Norris 2004; D'Antona et al. 2005) postulated to explain the observed split among the main-sequence stars of ω Cen and NGC 2808 (Bedin et al. 2004; Piotto et al. 2005, 2007). D'Antona & Ventura (2007) propose a model in which stars born with some helium-enrichment experience non-canonical deep mixing on the red giant branch, which increases their helium abundance to values of $Y > 0.5$, reaching values of 0.6...0.7 for special extra-mixing formalisms (D'Antona, priv. comm). The concept of helium-enriched sub-populations in globular clusters has been extended to the point where some authors claim that most, if not all, globular clusters contain *highly* helium-enriched populations (e.g. D'Antona & Caloi 2008; Caloi & D'Antona 2008, [M 3], Di Criscienzo et al. 2010 [NGC 6397]). On the other hand, Catelan et al. (2009) use high-precision observations of M 3 HB stars to rule out helium enhancement of $\Delta Y \gtrsim 0.02$. Villanova et al. (2009) attempted to determine the helium abundance of a globular cluster with a very extended horizontal branch (NGC 6752), but found no evidence of helium enhancement in HB stars between 8500 K and 9000 K[1]. However, as their targets are Na-poor and O-rich and therefore unlikely to be helium enriched, this result is inconclusive. Sandquist et al. (2010) in a very extensive study of the globular cluster M 13 found no evidence of the significant helium enrichment claimed by Caloi & D'Antona (2005) and D'Antona & Caloi (2008). Portinari et al. (2010) suggested that the stellar evolution models of the lower main sequence do not predict the correct relation between effective temperature and helium content. Evolutionary models constructed for a canonical helium content suggest a helium-to-metal enrichment ratio of $\Delta Y/\Delta Z = 10$ for local stars on the lower main sequence. This ratio would imply a helium content significantly smaller than the primordial helium abundance ($Y \approx 0.1$) for the most metal-poor local stars. On the other hand, empirical relations reproducing the observed behaviour of local lower main-sequence stars for $\Delta Y/\Delta Z = 2$ suggest a lower helium enrichment for the globular clusters ω Cen and NGC 2808, thereby reducing the problems in achieving that enrichment.

For an excellent review of the rôle of helium enrichment in the problem of the second parameter we refer to Gratton et al. (2010). They argue that a moderate helium enrichment of $\Delta Y < 0.1$ represents a third parameter (in addition to the second parameter, age). While ω Cen is unfortunately not part of their study they analyse many of the blue-hook globular clusters mentioned earlier. This moderate value is also supported by the analysis of the red giant branch stars in 19 globular clusters from the Gratton et al. sample by Bragaglia et al. (2010).

Lee et al. (2005) suggested that the blue hook stars are the progeny of the proposed helium-rich main-sequence stars in ω Cen. D'Antona et al. (2010) proposed that two populations of very helium-rich HB stars ($Y = 0.8$ and $Y = 0.65$, corresponding to $\log \frac{n_{\rm He}}{n_{\rm H}} = 0$ and -0.33, respectively), which achieve their extreme abundances via extra mixing processes during the red giant branch evolution of $Y \approx 0.4$ stars, could explain the observations of blue hook stars in ω Cen. If the blue hook stars were to be explained *solely* by the helium-enrichment scenario, their helium abundance should therefore not exceed $Y \approx 0.8$ and carbon should not be enriched at all. Spectroscopic observations of the blue (and supposedly helium-rich) main-sequence stars in ω Cen yielded a carbon abundance of [C/M] = 0.0 (Piotto et al. 2005). This carbon abundance will decrease further as the stars ascend the red giant branch, due to the extra-mixing process that occurs in metal-poor red giants (Kraft 1994; Gratton et al. 2000). Origlia et al. (2003) confirmed that the RGB stars in ω Cen have the low ^{12}C/^{13}C ratios ($\approx$4) and low average carbon abundances ([C/Fe] = -0.2) expected from this extra mixing. Thus the helium-enrichment scenario predicts a carbon abundance by mass in the blue hook stars of less than 0.1%, i.e., at least a factor of 10 smaller than the carbon abundance predicted by the flash-mixing scenario. A UV study of five massive globular clusters with blue hook stars by Brown et al. (2010) also showed that the faint luminosities observed for these stars can only be explained by the late hot flasher scenario. However, neither of the two scenarios can explain the range of colours observed for blue hook stars, especially in the more metal-rich globular clusters. Also Dalessandro et al. (2011) are unable to reproduce the UV and optical photometry of the blue hook stars in NGC 2808 solely with helium enrichment.

Previous spectra of the blue hook stars in ω Cen (Moehler et al. 2002) and NGC 2808 (Moehler et al. 2004) showed that these stars are indeed both hotter and more helium-rich than the canonical EHB stars. However, the blue hook stars show evidence for considerable amounts of hydrogen. Unfortunately, due to the limited resolution and signal-to-noise ratios (S/N) of the available data we have been unable to derive reliable abundances for C and N. We could instead only state that the most helium-rich stars appear to show some evidence of C/N enrichment. We

[1] Fabbian et al. (2005) also presented helium abundances for two HB stars in NGC 1904 that lie redward of the diffusion threshold, but their error bars of ± 0.3 dex prohibit any conclusion about helium enhancement.

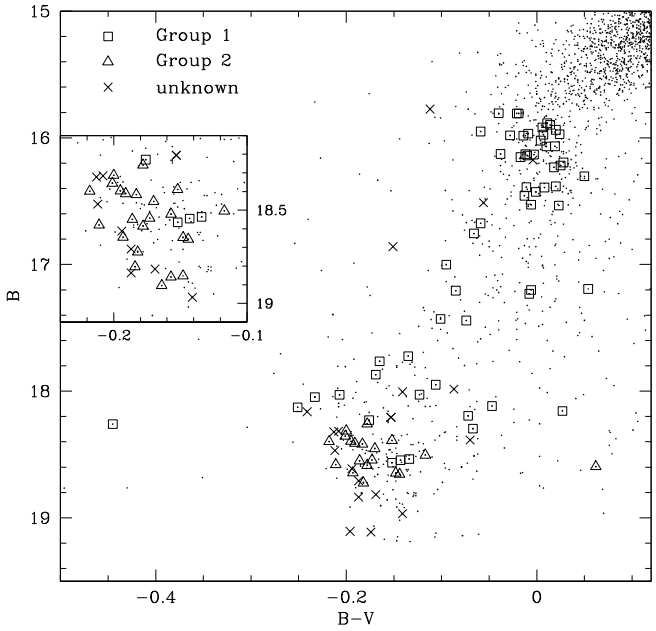

Fig. 1. $B, B-V$ colour–magnitude diagram with the FLAMES targets marked. "Unknown" refers to targets where the spectra did not allow an analysis. See text for details.

therefore started a project to obtain higher resolution spectra of hot and extreme HB stars and blue hook stars in ω Cen. Our first results were published in Moehler et al. (2007).

2. Observations

We selected stars along the blue HB in ω Cen from the multiband (U, B, V, I) photometry of Castellani et al. (2007), observed with the Wide Field Imager at the 2.2 m MPG/ESO telescope. These data together with multiband data from the Advanced Camera for Surveys onboard the Hubble Space Telescope provided the largest sample of HB stars (≈3200) ever collected for a globular cluster. Among them we concentrated on the stars at the faint end of the HB, which are the most likely "blue hook" candidates as shown by Moehler et al. (2002, 2004). To avoid crowding problems, we tried to select only isolated stars. The astrometry was performed using the UCAC2 catalog (Zacharias et al. 2004), which does not cover the central crowded regions. However, thanks to the large field covered by the current data set the astrometric solution is based on ≈3000 objects with an rms error of 0.″06. The targets are marked in Fig. 1 and listed in Table 1.

The spectroscopic data were obtained in 2005 (4 observations) and in 2006 (5 observations) in Service Mode using the MEDUSA mode of the multi-object fiber spectrograph FLAMES+GIRAFFE on the UT2 Telescope of the VLT. We used the low spectroscopic resolution mode with the spectral range 3964 Å–4567 Å (LR2, R = 6400) and observed spectra for a total of 109 blue hook and canonical blue HB/EHB star candidates (see Table 1) and for 17 sky background positions. Each observation had an exposure time of 2550 s to keep the total execution time of the observing block shorter than one hour. Table 2 lists the observing conditions. Unfortunately, only 9 of 20 planned observations could be obtained, which limits the S/N especially for the fainter stars.

Table 1. Target coordinates, heliocentric radial velocities, and B brightness.

Number	α_{2000}	δ_{2000}	B	RV [km s^{-1}]
24609[1]	13:25:34.3	−47:29:50.0	18.708	254.0
25751[1]	13:25:35.6	−47:27:45.3	18.836	197.8
26774	13:25:36.6	−47:31:07.9	18.645	213.0
29850	13:25:39.8	−47:28:57.0	18.411	240.0
30675	13:25:40.5	−47:33:27.7	17.206	220.0
31400	13:25:41.3	−47:29:06.3	18.803	227.6
32033[2]	13:25:42.0	−47:25:38.7	15.773	258.6
35357	13:25:45.0	−47:36:47.5	15.806	233.0
35828	13:25:45.5	−47:28:27.9	18.229	199.5
36669	13:25:46.5	−47:22:36.6	18.127	205.6
36725	13:25:46.4	−47:26:52.2	18.967	241.0
39876[1]	13:25:49.1	−47:36:04.0	18.316	–
40846	13:25:50.0	−47:29:45.3	18.417	255.3
41074	13:25:50.1	−47:32:06.3	18.521	227.7
43148[1]	13:25:51.9	−47:31:39.4	18.468	227.1
43520	13:25:52.3	−47:22:57.8	18.580	227.4
45556	13:25:53.8	−47:34:48.7	18.398	222.0
45715[3]	13:25:54.0	−47:29:07.8	16.512	–
45734[1]	13:25:54.0	−47:35:21.6	18.612	255.4
51341	13:25:58.6	−47:23:50.8	15.808	207.1
51359	13:25:58.5	−47:30:59.8	18.595	218.5
53022[1]	13:25:59.8	−47:37:45.8	18.322	266.7
53367[4]	13:26:00.1	−47:35:17.5	19.112	209.1
53945	13:26:00.7	−47:29:28.3	18.724	203.7
54733	13:26:01.4	−47:22:36.8	18.858	217.4
55158	13:26:01.5	−47:35:43.8	18.396	251.7
56896	13:26:03.0	−47:20:29.3	18.258	236.2
58774	13:26:04.3	−47:31:32.7	18.296	216.9
59125	13:26:04.6	−47:30:21.9	15.807	231.0
59786	13:26:05.2	−47:21:44.9	18.585	229.2
60820	13:26:05.8	−47:29:25.2	18.029	226.7
65373	13:26:08.8	−47:37:12.6	18.355	232.3
66104[3]	13:26:09.4	−47:29:57.5	15.593	–
66703[1]	13:26:09.8	−47:25:10.7	18.162	187.7
67933[1]	13:26:10.5	−47:39:09.9	18.896	–
69373	13:26:11.5	−47:27:51.5	17.870	219.3
71099	13:26:12.6	−47:36:13.8	19.107	264.3
72787	13:26:13.8	−47:30:58.2	15.917	211.5
74069[4]	13:26:14.6	−47:26:47.5	16.859	229.4
75364	13:26:15.5	−47:25:03.0	18.904	220.2
75981[4]	13:26:15.9	−47:28:09.2	18.313	211.5
75993[4]	13:26:15.9	−47:28:30.4	18.206	220.3
80690	13:26:19.0	−47:20:20.3	18.453	217.5
80711	13:26:18.9	−47:25:09.1	15.898	220.4
81395	13:26:19.4	−47:22:17.1	15.884	220.1
81722	13:26:19.6	−47:28:49.0	16.304	239.1
82860	13:26:20.4	−47:20:14.1	15.983	228.7
86429	13:26:22.6	−47:30:52.9	17.201	206.1
87161	13:26:23.0	−47:39:36.6	18.543	236.2
87175	13:26:23.1	−47:26:10.3	16.132	235.5
87734	13:26:23.5	−47:21:54.5	16.140	215.5
89495	13:26:24.8	−47:23:25.2	15.937	207.2
92333[4]	13:26:26.7	−47:31:05.7	17.193	213.9
93516	13:26:27.6	−47:21:13.7	16.022	226.0
95401	13:26:28.9	−47:36:20.8	18.536	212.2
96242	13:26:29.6	−47:20:44.5	16.176	216.6

Table 1. continued.

Number	α_{2000}	δ_{2000}	B	RV [km s^{-1}]
102600	13:26:34.1	−47:20:57.5	17.723	213.0
102850	13:26:34.3	−47:23:20.3	16.383	233.5
103563	13:26:34.7	−47:40:24.8	18.028	205.2
111785	13:26:40.5	−47:20:44.5	19.141	239.2
112475	13:26:40.9	−47:18:42.6	18.504	232.6
114491	13:26:42.3	−47:37:29.5	16.528	223.3
115087	13:26:42.7	−47:36:33.8	16.534	235.3
115194	13:26:42.8	−47:21:18.0	18.117	229.0
120119	13:26:46.2	−47:22:49.7	18.852	230.2
120901[4]	13:26:46.8	−47:33:29.0	18.987	216.5
124014[4]	13:26:48.9	−47:33:30.1	19.036	226.0
125302	13:26:49.7	−47:21:52.3	16.233	228.6
126350	13:26:50.5	−47:22:05.8	17.231	227.3
126892	13:26:50.9	−47:37:10.5	18.389	229.4
130310	13:26:53.1	−47:36:13.0	15.981	244.9
130831	13:26:53.5	−47:33:09.8	16.195	244.4
133846	13:26:55.3	−47:35:57.4	16.129	221.5
135227[4]	13:26:56.2	−47:34:36.8	18.816	205.5
137299	13:26:57.4	−47:22:59.5	17.949	217.3
141008	13:26:59.8	−47:21:14.0	18.646	226.9
144749[4]	13:27:02.2	−47:25:45.2	18.386	238.2
145078[3]	13:27:02.4	−47:25:10.6	17.984	–
147746	13:27:04.2	−47:35:02.3	15.967	226.3
147880	13:27:04.3	−47:34:25.4	15.950	234.0
148641[4]	13:27:04.7	−47:23:02.8	19.815	210.8
156459	13:27:10.2	−47:27:33.8	15.975	210.9
161310[1]	13:27:13.7	−47:39:23.6	18.047	234.6
162839	13:27:14.6	−47:24:07.4	16.390	224.6
164808	13:27:16.1	−47:34:01.6	18.549	222.2
165244	13:27:16.5	−47:39:28.4	15.972	232.2
169814	13:27:19.8	−47:26:55.3	16.392	233.5
170215	13:27:20.2	−47:36:06.5	16.068	221.7
170450[1]	13:27:20.5	−47:38:41.8	18.005	236.4
171696	13:27:21.3	−47:27:18.0	16.067	243.3
172332	13:27:21.7	−47:23:44.6	16.427	242.6
174389	13:27:23.6	−47:32:31.0	16.152	236.0
177314	13:27:26.0	−47:32:42.6	17.442	219.8
180375	13:27:28.7	−47:30:34.5	16.218	214.2
180714[4]	13:27:29.1	−47:34:59.6	18.156	221.3
181678	13:27:29.8	−47:24:21.8	18.599	244.2
182005	13:27:30.3	−47:32:23.8	16.457	228.3
182772	13:27:31.0	−47:27:16.9	17.764	237.3
183592	13:27:32.0	−47:28:55.2	18.195	233.3
186476	13:27:36.2	−47:32:41.8	18.545	236.3
187534	13:27:37.9	−47:30:30.9	18.260	217.9
188882	13:27:40.4	−47:34:02.4	17.001	219.0
189080	13:27:40.8	−47:31:53.5	18.511	235.6
190398	13:27:43.3	−47:27:00.5	18.656	233.8
190635	13:27:43.8	−47:27:23.0	16.675	239.3
191111	13:27:44.7	−47:25:19.8	18.565	225.0
191969	13:27:46.7	−47:33:15.5	16.127	227.5
193486	13:27:50.3	−47:32:17.6	16.755	224.4
194383	13:27:52.6	−47:27:39.0	17.430	217.3

Notes. [(1)] Very noisy spectra; [(2)] only 2 spectra extracted; [(3)] no spectra extracted; [(4)] G-band and/or Fe I 4325 Å visible.

3. Data reduction

For our first analysis presented in Moehler et al. (2007), we used the ESO pipeline-reduced data. Unfortunately the pipeline version used for those data did not correct for the bright spot seen at the upper right corner of the GIRAFFE CCD. Therefore we reduced the data again using the Geneva pipeline GirBLDRS[2] (version 1.11). To remove the bright spot from the data we obtained raw dark frames from the ESO archive[3] for the time range covered by our data. First we created master bias frames by averaging the five bias frames that had been obtained for each observation. Then the three dark frames observed on a given date were bias corrected and averaged with cosmic ray rejection. To reduce the noise in the dark frames, we smoothed them with a 2×2 pixel box filter. We then used the three flat fields observed for each night to determine the positions of the spectra. We did not correct these data for dark current, as the bright spot showed no negative effect on the detection of the spectra. Afterwards we derived the full wavelength solution from the ThAr arc frames observed for each date. Using this solution, we finally extracted and rebinned the science data. At this step we included the smoothed master dark frames. The wavelength calibration was adjusted using the simultaneously observed ThAr spectra. As the optimal extraction produced spectra of lower signal-to-noise than conventional averaging we used the average option to integrate the flux for each spectrum. We also divided the spectra by extracted flat-field spectra to perform a first correction for the CCD sensitivity variations. Unfortunately, no flux standard stars are observed by GIRAFFE in the MEDUSA mode, which would permit at least a relative flux calibration to be obtained.

For each exposure, we subtracted the median of the spectra from the sky fibers from the extracted spectra of the target stars. We corrected all spectra for barycentric motion. During this correction, we noted that we had made a sign error when performing this correction for the data published by Moehler et al. (2007). This error led to a smearing of the line profiles in the averaged spectra.

When comparing spectra observed at different dates, we found that the slope of the extracted spectra tends to vary from one observation to the next. To average the spectra, we therefore first normalized the individual spectra. To achieve this we fitted a 5th order polynomial to regions free from strong lines (4000–4020 Å, 4040–4070 Å, 4160–4300 Å, 4410–4440 Å, and 4510–4550 Å). In Fig. 2, we show example fits for helium-poor and helium-rich stars.

Table 2. Observing log.

Start of exposure UT	Airmass	Seeing [″]	Moon illum.	Moon dist. [°]
2005-04-04T02:53:11.238	1.204	0.61	0.264	89.9
2005-04-10T07:55:31.608	1.444	0.49	0.027	146.3
2005-04-11T08:03:46.508[1]	1.420	1.09	0.071	145.4
2005-04-16T02:15:02.180	1.187	0.88	0.445	109.5
2005-04-17T07:30:33.470	1.455	0.77	0.560	97.4
2006-04-02T05:00:55.927	1.089	0.67	0.181	142.9
2006-06-15T23:13:58.802	1.112	0.62	0.780	97.2
2006-06-28T23:11:12.410	1.089	0.59	0.104	88.1
2006-06-30T01:37:27.558	1.245	1.08	0.177	76.8
2006-07-04T00:55:50.945	1.190	0.78	0.528	40.8
2006-08-09T23:31:50.834	1.349	1.59	0.994	101.2
2006-08-09T23:25:30.528	1.261	1.51	0.994	101.1

Notes. The seeing given is that measured by the DIMM. The true seeing at the UT is often better. [(1)] Exposure aborted after 11 min.

[2] http://girbldrs.sourceforge.net/
[3] http://archive.eso.org/wdb/wdb/eso/giraffe/form

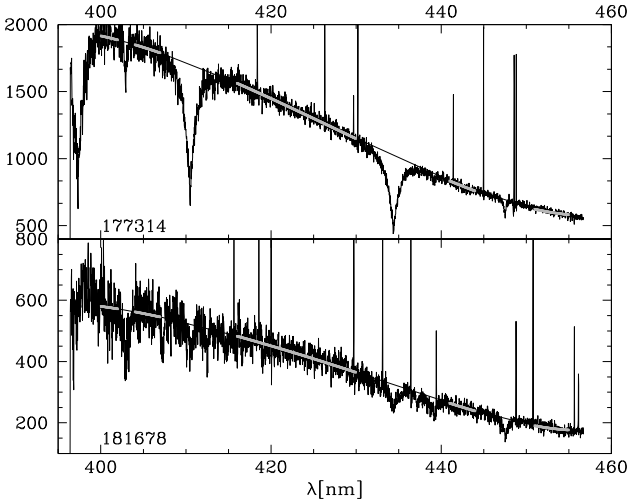

Fig. 2. Spectra and fits to them from April 2, 2006, for a helium-poor star (*top*) and a helium-rich star (bottom). The regions used for the fit are marked in grey.

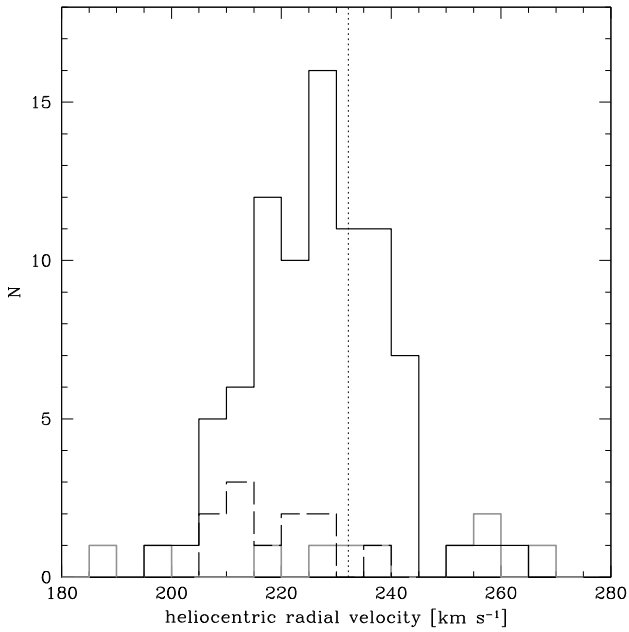

Fig. 3. The distribution of heliocentric radial velocities. The solid black line shows the distribution for spectra with no notation in Table 1, the dashed black line shows the distribution for spectra showing a G-band and the solid grey line shows the distribution for noisy spectra. The heliocentric radial velocity of ω Cen is marked by the dotted line at 232.2 km s^{-1} (Harris 1996).

4. Radial velocities

After the barycentric correction, the observed spectra were – in a first step – cross-correlated with synthetic spectra roughly matching the stellar parameters, i.e. helium abundance, surface gravity, and effective temperature. Only regions of hydrogen or helium lines were selected prior to the cross-correlation. The peak of the cross-correlation function was then fitted with a Gaussian function to determine the radial velocity to sub-resolution accuracy. The velocity-corrected spectra were then co-added and fitted with synthetic model atmospheres (see Sect. 5). In a second step, the best-fit synthetic spectra were then used to repeat the cross-correlation. Figure 3 shows the distribution of the radial velocities. The median radial velocity of the 83 "clean" target stars (i.e. with sufficient signal and without G-band[4]) of 226.8 km s^{-1} derived this way differs by 5.4 km s^{-1} from the accepted value for ω Cen of 232.2 km s^{-1} (Harris 1996). Using a more sophisticated approach that accounts for the uncertainties in the individual measurements and fits a Gaussian to the velocity distribution of *all* target stars with measurable radial velocities, we derive a marginally lower heliocentric radial velocity of 226.5 km s^{-1} and a standard deviation σ of 17.4 km s^{-1}.

The mean and standard deviation of the radial velocity were determined from the up to nine individual spectra for each object. This standard deviation was compared to the standard deviation in the spectral flux, calculated from a continuum region between 4150 and 4250 Å. By comparing these two quantities we found a linear dependence of the scatter in the radial velocity measurements for each star on the quality of the spectra (see Fig. 4). The plot includes the linear fit to the good data as well as the 2 σ-limits. Stars with a significantly higher scatter might be primary stars within a binary, where the scatter represents orbital motions with periods smaller than the duration of the observing campaign. Ignoring the few stars with very poor spectra, i.e. with a spectral standard deviation in flux above 0.1, we identify five objects that may be binary members.

For each target star, we fitted sine curves by stepping through test periods from 1 to 230 days adopting the standard deviation of the radial velocity measurements as the amplitude, the mean as the velocity offset, and an arbitrary phase as a starting approximation. The amplitude, period, and phase were allowed to vary during the fit procedure. The period belonging to the fit with the lowest standard deviation in the residuals was taken as possible binary period. For each object, we then created a series of radial velocity curves with identical times but randomly distributed radial velocity measurements with a standard deviation equaling that of the RV measurements. Each of these curves was then fitted with the previously determined possible period. We counted the fits with amplitudes smaller than that of the original light curve to derive a false alarm probability. Out of our sample, 21 objects have a false alarm probability below 5%. However, none of these experience a significant reduction in standard deviation between the original RV measurements and the residuals for the best-fit period. Among these 21, there is also no overlap with the five objects showing an excess RV standard deviation with respect to the spectral S/N. We therefore conclude that we cannot reliably identify spectroscopic binaries within our sample.

After verifying that there were no significant radial velocity variations, we then averaged the individual spectra for each star, excluding at each wavelength the two highest and the two lowest data points. Usually this meant that 5 data points were used to compute the average. However, some stars could not be extracted in all exposures or had data of too-low S/N to determine a radial velocity. In these cases, the number of data points available for averaging was obviously smaller. This affected the stars 36725 (2 spectra), 45734 (3 spectra), 190635 (4 spectra), 43148, 53022, 53945, 66703, 71099 (5 spectra each), 55158, 75364 164808 (6 spectra each), 24609, 170450, 182005 (7 spectra each), and 25751, 80690, 112475, 162839, 180375, 180714, 182772, 188882, 190398, and 191111 (8 spectra each). To check if the stars with fewer spectra had significantly lower

[4] The presence of a G-band in a hot star's spectrum indicates an optical or physical binary with a cool companion.

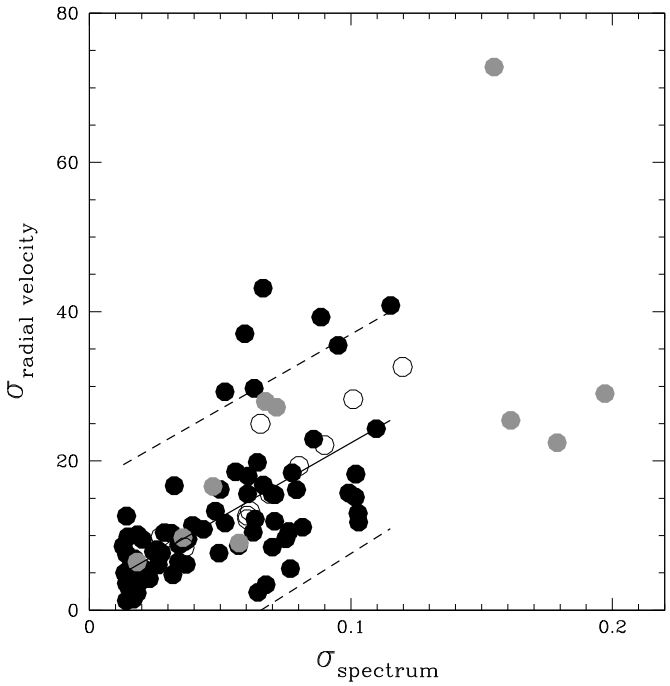

Fig. 4. The scatter in the radial velocities from individual spectra versus the signal-to-noise ratio of the spectra. The solid black dots are from spectra with no annotation in Table 1 (i.e. good spectra), the grey dots are from noisy spectra, and the open symbols refer to spectra containing a G band.

S/N we fitted the S/N of the spectra determined between 420 nm and 423 nm versus the B magnitude for stars with nine spectra available for averaging. We found that the S/N of the stars with fewer spectra is within $\pm 2\sigma$ ($\pm 50\%$) of this fit for all stars with $B \lesssim 18.4$. For fainter stars (24609, 25751, 43148, and 45734), the lack of spectra yields averaged spectra with a S/N below 12 in the studied region, which is the empirical limit for a meaningful analysis within this data set. There are, however, also two objects with nine spectra that are below this limit: 39876 and 67933.

5. Analysis

5.1. Atmospheric parameters

To derive effective temperatures, surface gravities, and helium abundances, we fitted the Balmer lines H_γ and H_δ (and/or the He II lines at these positions) and the He I lines 4026 Å, 4388 Å, and 4471 Å.

To establish the best fit to the observed spectra, we used the routines developed by Bergeron et al. (1992) and Saffer et al. (1994), as modified by Napiwotzki et al. (1999), which employ a χ^2 test. The σ necessary for the calculation of χ^2 is estimated from the noise in the continuum regions of the spectra. The fit program normalizes both the model *and* observed spectra using the same points for the continuum definition.

Recent tests have shown, however, that these fit routines underestimate the *formal* errors by at least a factor of 2 (Napiwotzki priv. comm.). We therefore provide formal errors multiplied by 2 to account for this effect. In addition, the errors provided by the fit routine do not include possible systematic errors caused by, e.g., flat-field inaccuracies or imperfect sky subtraction. The true errors in $T_{\rm eff}$ are probably close to 5% at least, and the true errors in $\log g$ are probably about 0.1.

The spectra were fitted with various model atmospheres. As the late hot flasher scenario predicts enrichment in carbon and nitrogen, an extensive grid of *non-LTE line-blanketed* model atmospheres has been produced with the NLTE model atmosphere code TLUSTY[5] (Hubeny & Lanz 1995). These model atmospheres allow for departures from LTE for 1132 explicit levels and superlevels of 52 ions (H, He, C, N, O, Ne, Mg, Al, Si, P, S, Fe). A detailed description of the model atoms and the source of the atomic data can be found in Lanz & Hubeny (2003, 2007). The model grid covers the range of stellar parameters typical of EHB stars: 20 000 K $\leq T_{\rm eff} \leq$ 50 000 K (step of 2500 K), 4.75 $\leq \log g \leq$ 6.5 (step of 0.25 dex), and $-3 \leq \log \frac{n_{\rm He}}{n_{\rm H}} \leq +2$ (step of 1 dex) at a microturbulent velocity, $\xi = 5$ km s^{-1}. For each model atmosphere with $\log \frac{n_{\rm He}}{n_{\rm H}} \geq -1$, we calculated a second model with *enriched content of carbon and nitrogen* (marked by $^{\rm C}$ in Table 4) following the prediction of the "flash mixing" scenario, adopting mass fractions of 3% and 1% for carbon and nitrogen, respectively (Lanz et al. 2004). We adopted scaled-solar abundances at ω Cen's dominant metallicity ([Fe/H] = − 1.5). This abundance ratio by numbers was kept the same for all models, including helium-rich models, which implies that the heavy element mass fraction differs for models with different helium (and C, N) content. We emphasize, however, that the abundance of iron-peak elements in EHB stellar photospheres is unknown and probably affected by diffusion processes. Furthermore, the low abundance of heavy elements limits the effect of metal line blanketing on the atmospheric structure and the predicted emergent spectrum. Therefore, the resulting uncertainty in our analysis caused by assuming the same [Fe/H] value remains small. Once the atmospheric structure of each model atmosphere converged, we calculated detailed emergent spectra in the $\lambda\lambda$3800–4600 Å range with the spectrum synthesis code, SYNSPEC, using the NLTE populations calculated by TLUSTY.

For the helium-poor stars above 20 000 K, we also used the TLUSTY models. For the cooler stars, we used *metal-rich helium-poor LTE* models (Moehler et al. 2000).

Using the atmospheric parameters, a distance modulus of $(m - M)_0 = 13\overset{\rm m}{.}45$, and an interstellar absorption of $A_V = 0\overset{\rm m}{.}47$, we derived masses for our target stars as described in Moehler et al. (2000). The masses for the helium-rich stars are somewhat underestimated as we used theoretical brightness values for solar-helium atmospheres, which are brighter in the optical range than helium-rich atmospheres.

The helium abundances plotted in Fig. 5 shows a clear distinction between helium-poor stars with $\log \frac{n_{\rm He}}{n_{\rm H}} < -1.6$ (open squares, Group 1 hereafter) and stars with helium abundances close to or above solar (filled triangles, Group 2 hereafter).

5.2. Spatial distribution

Moehler et al. (2007) noted an asymmetric spatial distribution of the helium-rich stars. To verify the significance of this effect, we investigated the spatial distribution of the faint HB stars, $B > 17$, adopting the combined Advanced Camera for Surveys (ACS) and wide field imager (WFI) photometric catalog (Castellani et al. 2007). We selected candidate helium-rich and helium-poor HB stars according to the magnitudes of the spectroscopically confirmed samples. We assumed helium-rich stars to be those with $B > 18.35$ and helium-poor stars to be those with $B \leq 18.35$. The spatial distribution of the two samples does

[5] http://nova.astro.umd.edu

Table 3. Atmospheric parameters for stars with sub-solar helium abundances

Number	χ^2	$T_{\rm eff}$	$\log g$	$\log \frac{n_{\rm He}}{n_{\rm H}}$
29850	1.105	33 400 ± 1000	5.87 ± 0.18	−1.28 ± 0.14
30675	1.583	16 400 ± 600	4.54 ± 0.10	−2.16 ± 0.16
32033	1.227	17 000 ± 600	4.09 ± 0.10	−1.52 ± 0.10
35357	1.137	13 200 ± 500	3.99 ± 0.12	−2.46 ± 0.40
35828	1.030	29 800 ± 1000	5.54 ± 0.18	−3.35 ± 0.12
36669	1.300	38 600 ± 1800	5.68 ± 0.20	−3.21 ± 0.38
40846	1.070	32 400 ± 1600	5.52 ± 0.26	−1.07 ± 0.18
45556	1.271	33 100 ± 1100	5.68 ± 0.20	−1.50 ± 0.14
51341	1.796	12 900 ± 200	3.90 ± 0.06	−2.57 ± 0.22
51359	1.310	32 400 ± 1100	5.62 ± 0.18	−1.20 ± 0.12
58774	1.354	25 900 ± 1700	5.27 ± 0.20	−3.14 ± 0.14
59125	2.350	13 400 ± 300	3.96 ± 0.06	−2.54 ± 0.20
60820	1.091	40 400 ± 1300	5.46 ± 0.12	−3.19 ± 0.16
65373	1.062	33 200 ± 900	5.69 ± 0.14	−1.00 ± 0.08
69373	1.122	30 100 ± 7800	5.48 ± 0.12	−3.26 ± 0.10
72787	1.182	13 700 ± 300	4.05 ± 0.06	−2.55 ± 0.16
75981	1.056	33 500 ± 1600	5.42 ± 0.26	−1.42 ± 0.16
80711	2.113	13 400 ± 200	4.03 ± 0.06	−2.63 ± 0.14
81395	1.227	13 400 ± 200	4.06 ± 0.04	−2.34 ± 0.10
81722	2.376	17 700 ± 700	4.18 ± 0.10	−1.90 ± 0.10
82860	2.789	14 900 ± 300	4.11 ± 0.06	−2.30 ± 0.12
86429	1.585	28 200 ± 1600	4.86 ± 0.18	−3.20 ± 0.16
87175	2.200	15 700 ± 300	4.16 ± 0.06	−2.91 ± 0.08
87734	2.588	14 100 ± 300	4.13 ± 0.06	−2.74 ± 0.16
89495	1.877	14 000 ± 300	4.00 ± 0.06	−2.54 ± 0.20
93516	2.920	14 300 ± 300	4.06 ± 0.06	−2.59 ± 0.16
95401	1.257	31 900 ± 1000	5.68 ± 0.20	−3.10 ± 0.18
96242	1.826	15 900 ± 400	4.15 ± 0.06	−2.44 ± 0.10
102600	1.172	28 600 ± 1000	5.25 ± 0.14	−3.13 ± 0.10
102850	1.852	16 300 ± 500	4.23 ± 0.08	−2.49 ± 0.12
103563	1.249	26 700 ± 1200	5.30 ± 0.14	−2.02 ± 0.12
112475	1.272	30 900 ± 1100	5.76 ± 0.20	−1.38 ± 0.14
114491	1.848	17 400 ± 500	4.44 ± 0.06	−2.57 ± 0.08
115087	1.826	18 300 ± 500	4.51 ± 0.06	−2.26 ± 0.06
115194	1.351	30 000 ± 8000	5.56 ± 0.12	−2.60 ± 0.12
125302	2.068	14 700 ± 300	4.10 ± 0.06	−2.54 ± 0.14
126350	1.325	24 100 ± 1000	4.99 ± 0.12	−1.79 ± 0.08
130310	3.165	14 100 ± 200	4.05 ± 0.06	−2.49 ± 0.14
130831	1.298	15 700 ± 500	4.09 ± 0.10	−2.96 ± 0.14
133846	2.828	14 200 ± 300	4.05 ± 0.06	−2.52 ± 0.18
137299	1.144	31 500 ± 6500	5.48 ± 0.12	−3.26 ± 0.08
141008	1.010	36 300 ± 1000	5.92 ± 0.16	−1.09 ± 0.14
147746	2.120	13 500 ± 300	3.97 ± 0.06	−2.67 ± 0.20
147880	2.743	14 000 ± 300	3.96 ± 0.06	−2.40 ± 0.18
156459	2.095	15 100 ± 500	4.06 ± 0.10	−1.93 ± 0.10
162839	1.616	15 700 ± 400	4.15 ± 0.06	−2.39 ± 0.12
164808	1.489	32 500 ± 1100	5.93 ± 0.18	−1.02 ± 0.14
165244	3.106	13 500 ± 300	4.04 ± 0.06	−2.94 ± 0.24
169814	2.328	15 200 ± 400	4.26 ± 0.08	−3.05 ± 0.16
170215	2.409	13 800 ± 200	4.10 ± 0.06	−2.89 ± 0.16
171696	2.158	14 600 ± 400	4.05 ± 0.08	−2.93 ± 0.16
172332	2.145	16 500 ± 400	4.36 ± 0.06	−2.60 ± 0.10
174389	1.603	14 800 ± 400	4.10 ± 0.08	−2.63 ± 0.16
177314	1.109	19 200 ± 900	4.89 ± 0.10	−2.46 ± 0.10
180375	2.177	17 600 ± 500	4.21 ± 0.06	−2.42 ± 0.10
182005	1.628	15 800 ± 400	4.25 ± 0.06	−2.30 ± 0.10
182772	1.093	35 100 ± 7100	5.50 ± 0.12	−2.57 ± 0.12
183592	1.387	28 600 ± 1400	5.48 ± 0.16	−2.50 ± 0.16
186476	1.048	30 400 ± 1000	5.63 ± 0.18	−3.27 ± 0.18
187534	1.090	43 000 ± 1800	5.89 ± 0.20	−3.00 ± 0.28
188882	1.375	17 600 ± 600	4.62 ± 0.08	−2.76 ± 0.10
190635	1.988	17 300 ± 900	4.45 ± 0.14	−2.00 ± 0.12
191111	0.964	28 500 ± 2400	5.50 ± 0.32	−2.85 ± 0.26
191969	1.884	14 100 ± 300	4.12 ± 0.06	−2.28 ± 0.14
193486	1.117	17 500 ± 600	4.61 ± 0.08	−2.41 ± 0.12
194383	1.083	23 900 ± 1200	5.06 ± 0.14	−2.42 ± 0.10

Table 4. Atmospheric parameters for stars with super-solar helium abundances as derived with TLUSTY atmospheres.

number	χ^2	$T_{\rm eff}$	$\log g$	$\log \frac{n_{\rm He}}{n_{\rm H}}$
26774	1.128	31 100 ± 1400	5.97 ± 0.26	−0.54 ± 0.14
26774^C	1.083	30 300 ± 1500	6.03 ± 0.28	−0.72 ± 0.14
31400	1.338	31 600 ± 900	5.96 ± 0.18	−0.35 ± 0.10
31400^C	1.393	32 300 ± 900	6.03 ± 0.18	−0.46 ± 0.10
41074	1.450	31 100 ± 800	5.83 ± 0.14	−0.47 ± 0.08
41074^C	1.428	32 000 ± 900	5.96 ± 0.16	−0.53 ± 0.08
43520	1.113	33 700 ± 900	5.89 ± 0.14	−0.74 ± 0.08
43520^C	1.375	34 700 ± 1100	6.06 ± 0.20	−0.83 ± 0.08
53945	1.277	34 600 ± 1600	5.97 ± 0.26	−0.82 ± 0.16
53945^C	1.215	35 800 ± 2000	6.10 ± 0.30	−0.81 ± 0.16
54733	1.021	34 900 ± 1300	6.02 ± 0.20	−0.03 ± 0.12
54733^C	1.008	34 400 ± 1000	6.00 ± 0.20	−0.16 ± 0.12
55158	1.937	32 500 ± 1000	5.83 ± 0.18	−0.53 ± 0.12
55158^C	2.068	33 100 ± 1200	5.88 ± 0.24	−0.69 ± 0.14
56896	0.991	31 900 ± 900	5.74 ± 0.12	−0.67 ± 0.08
56896^C	1.256	33 900 ± 900	5.96 ± 0.16	−0.72 ± 0.08
59786	1.162	31 600 ± 1000	5.91 ± 0.18	−0.60 ± 0.10
59786^C	1.244	32 500 ± 1000	6.01 ± 0.20	−0.72 ± 0.12
75364	1.473	39 900 ± 1700	6.32 ± 0.24	−0.39 ± 0.16
75364^C	1.316	39 100 ± 1700	6.32 ± 0.26	−0.48 ± 0.16
80690	1.052	32 900 ± 900	5.90 ± 0.14	−1.02 ± 0.08
80690^C	1.166	33 300 ± 1000	6.03 ± 0.16	−1.19 ± 0.10
87161	1.112	33 800 ± 800	5.98 ± 0.14	−0.86 ± 0.08
87161^C	1.140	33 900 ± 900	6.11 ± 0.18	−1.00 ± 0.10
111785	1.421	40 500 ± 1000	5.85 ± 0.20	+0.88 ± 0.14
111785^C	1.235	35 900 ± 1400	6.28 ± 0.22	+0.68 ± 0.10
120119	1.515	33 800 ± 900	5.99 ± 0.16	−0.35 ± 0.10
120119^C	1.570	34 800 ± 900	6.07 ± 0.18	−0.45 ± 0.10
126892	1.202	31 500 ± 1500	5.47 ± 0.20	−0.80 ± 0.12
126892^C	1.275	33 000 ± 1300	5.71 ± 0.22	−0.88 ± 0.12
181678	1.497	42 400 ± 700	6.27 ± 0.18	+0.18 ± 0.12
181678^C	1.298	42 100 ± 700	6.42 ± 0.18	+0.10 ± 0.12
189080	1.430	33 800 ± 900	5.93 ± 0.16	−0.44 ± 0.10
189080^C	1.416	34 700 ± 1000	6.07 ± 0.20	−0.54 ± 0.10
190398	1.180	35 900 ± 1100	5.93 ± 0.16	−0.79 ± 0.10
190398^C	1.238	36 700 ± 1200	6.05 ± 0.20	−0.88 ± 0.10

Notes. $^{(C)}$ Indicates the use of C/N enhanced model atmospheres, whereas no notation indicates the use of model atmospheres using the cluster metallicity.

not exhibit any significant asymmetry in the four quadrants of the cluster. There is mild evidence of an overabundance of hot HB stars in general in the southeast quadrant of ω Cen (about 29% versus 22–25% in the other quadrants), but it is within the mutual error bars. On the other hand, the spectroscopically confirmed *helium-rich* EHB stars are concentrated in the northwest quadrant of the cluster, for which Calamida et al. (2005) found a lack of stars with lower than average reddening for $u - y$ and $V - I$. We are unable to draw a firm conclusion about the spatial

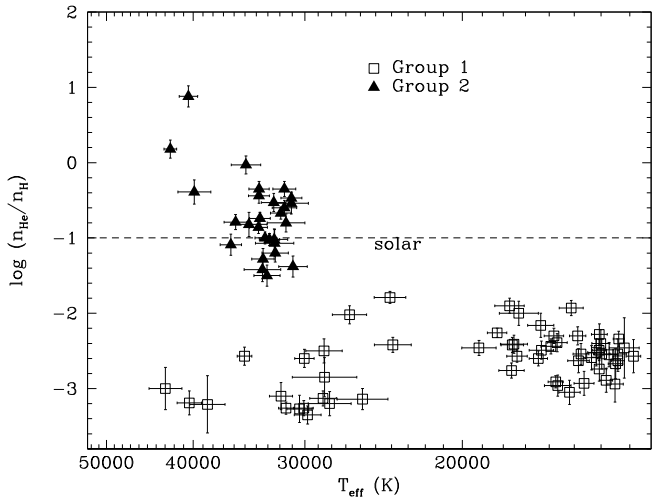

Fig. 5. The effective temperatures and helium abundances by number derived for our target stars (formal errors multiplied by 2, see text for details). Helium-poor and helium-rich stars are marked by open squares and filled triangles, respectively. The stars with super-solar helium are shown with the parameters derived from models without C/N enhancement. The dashed line indicates the solar helium abundance.

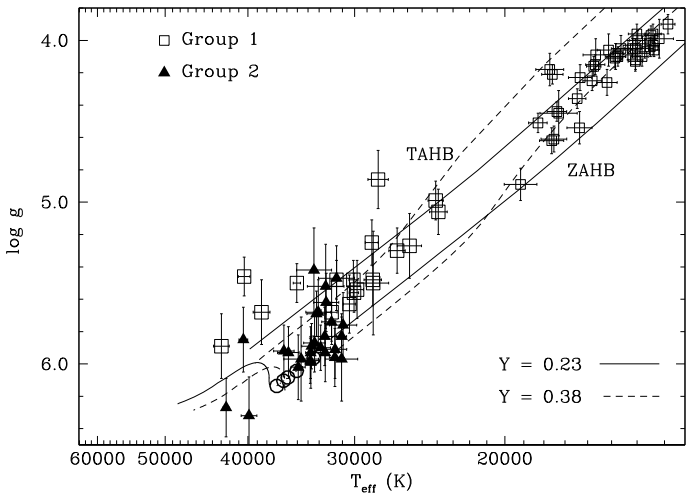

Fig. 6. The effective temperatures and surface gravities derived for our target stars (formal errors multiplied by 2, see text for details). Helium-poor and helium-rich stars are marked by open squares and filled triangles, respectively. The stars with super-solar helium are shown with the parameters derived from models without C/N enhancement. The solid lines mark the canonical HB locus ($Y = 0.23$) and the dashed lines mark the helium-enriched HB locus ($Y = 0.38$, see text for details). The tracks for a late hot flasher (same line types as for the ZAHB) show the evolution of these stars from the zero-age HB (ZAHB) towards helium exhaustion in the core (terminal-age HB = TAHB). The dotted line connects the series of ZAHB models computed by adding a hydrogen-rich layer to the surface of the canonical ZAHB model of the late hot flasher. The open circles mark – with decreasing temperature – hydrogen layer masses of 0, 10^{-7}, 10^{-6}, 10^{-5}, and 10^{-4} $M_{\odot}$ (for details see Moehler et al. 2002).

distribution of the helium-rich EHB stars because we lack sufficiently good statistics.

6. Evolutionary tracks

To compare the atmospheric parameters of our target stars with the theoretical models, we computed two sets of stellar evolutionary sequences: one with a helium-normal composition of $Y = 0.23$ and another with a helium-rich composition of $Y = 0.38$. The observed splitting of the main sequence in ω Cen indicates that the helium abundance in the blue main sequence (bMS) stars is larger by $\Delta Y \approx 0.15$ than the helium abundance in the red main sequence (rms) stars (Piotto et al. 2005). Thus our helium-normal and helium-rich sequences should represent the evolution of the rms and bMS stellar populations in ω Cen, respectively. The heavy element abundance Z for each of our two helium abundances was determined from the [Fe/H] values given by Piotto et al. (2005) and Villanova et al. (2007) for the rMS and bMS stars. Adopting [Fe/H] = −1.68 for the rMS stars and assuming an α element enhancement of [α/Fe] = 0.3, we found a scaled solar Z value of 0.00064 for our helium-normal composition. In obtaining this Z value, we used the prescription of Salaris et al. (1993) to convert an α-enhanced composition into the equivalent scaled solar composition. Using the same procedure, we obtained a scaled solar Z value of 0.0011 for our helium-rich composition from the [Fe/H] value of −1.37 for the bMS stars (Villanova et al. 2007).

Stellar models for both of our compositions were evolved continuously from the main sequence, up the RGB, through the helium flash to the ZAHB, and then through the HB phase. Mass loss was included during the RGB evolution according to the Reimers formulation, with the mass-loss parameter η_R being varied from 0 (no mass loss) up to the maximum value for which our models evolved to the ZAHB without undergoing flash mixing. The effective temperatures of these canonical ZAHB models at the hot end of the EHB were 32 000 K and 31 300 K, respectively, for our helium-normal and helium-rich compositions. Thus the higher helium abundance of our helium-rich composition did not increase the maximum effective temperature along the canonical ZAHB. We next computed additional sequences with higher mass-loss rates to determine the range in η_R over which flash mixing occurs. ZAHB models for the minimum, average, and maximum values of η_R leading to flash mixing were constructed assuming that all of the envelope hydrogen was burned during the mixing phase and that the envelope carbon abundance was increased to 0.04 by mass. These assumptions are consistent with the flash-mixing calculations of Cassisi et al. (2003) and Miller Bertolami et al. (2008). The average effective temperatures of the flash-mixed ZAHB models were 37 500 K and 35 900 K, respectively, for our helium-normal and helium-rich compositions. Thus both of these compositions predict a gap of ≈5000 K between the flash-mixed and the hottest canonical ZAHB models in good agreement with the earlier results of Brown et al. (2001). These flash-mixed ZAHB models were then evolved through the HB phase. Sequences with even higher mass-loss rates failed to ignite helium and thus died as helium white dwarfs.

7. Results and discussion

7.1. Helium-poor stars (Group 1)

The helium-poor stars plotted in Figs. 6 and 7 exhibit the same behaviour as hot HB stars and EHB stars in other globular clusters (see Moni Bidin et al. 2007, for a recent discussion). While comparing both effective temperature and surface gravity with the tracks implies helium enrichment, the too-low masses clearly indicate that the results are not trustworthy. As mentioned in

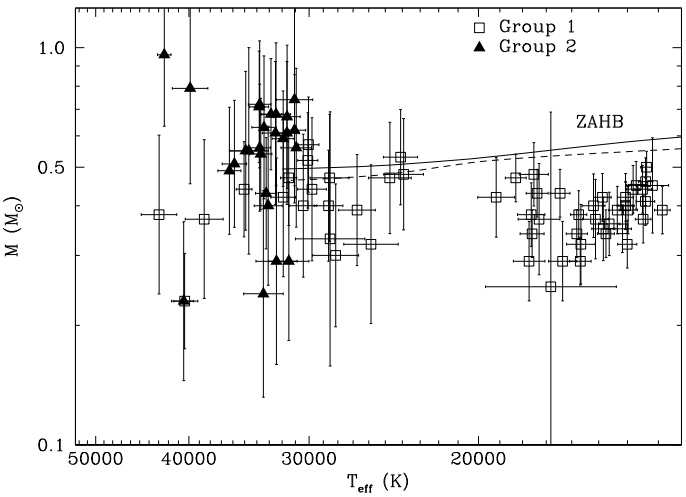

Fig. 7. The effective temperatures and masses derived for our target stars (formal errors multiplied by 2, see text for details). Helium-poor and helium-rich stars are marked by open squares and filled triangles, respectively. The stars with super-solar helium abundances are shown with the parameters derived from models without C/N enhancement. The lines mark the zero-age horizontal branch for $Y = 0.23$ (solid) and 0.38 (dashed, see text for details).

other papers, we suspect that the diffusion in the stars' atmospheres creates abundance ratios that are not correctly described by the model atmospheres we use.

It is noticeable, however, that all helium-poor stars with effective temperatures above 32 000 K (the end of the canonical ZAHB) have evolved away from the horizontal branch (cf. Fig. 6).

7.2. Helium-rich stars (Group 2)

The helium-rich stars cover the temperature range between the hot end of the ZAHB and the late hot flasher region. As already discussed by Moehler et al. (2007), diffusion acting in a late hot flasher would move any remaining hydrogen to the surface, while at the same time reducing the effective temperature. This behaviour is consistent with that observed in Figs. 5 and 6.

In Fig. 8, we show the spectra of the stars with super-solar helium abundance where the helium abundance decreases from top to bottom. We overplot model spectra with the cluster carbon and nitrogen abundance (dotted lines, mostly just horizontal) and with a carbon/nitrogen abundance of 3/1% by mass, respectively (solid black lines). The model spectra were derived by fitting the helium and hydrogen lines of the spectra, *not* the carbon lines. Obviously the most helium-rich stars show a strong tendency towards a high carbon abundance, which can so far only be explained by the late hot flasher scenario. This would also explain the rather abrupt change in helium abundance at effective temperatures hotter than the hot end of the canonical HB.

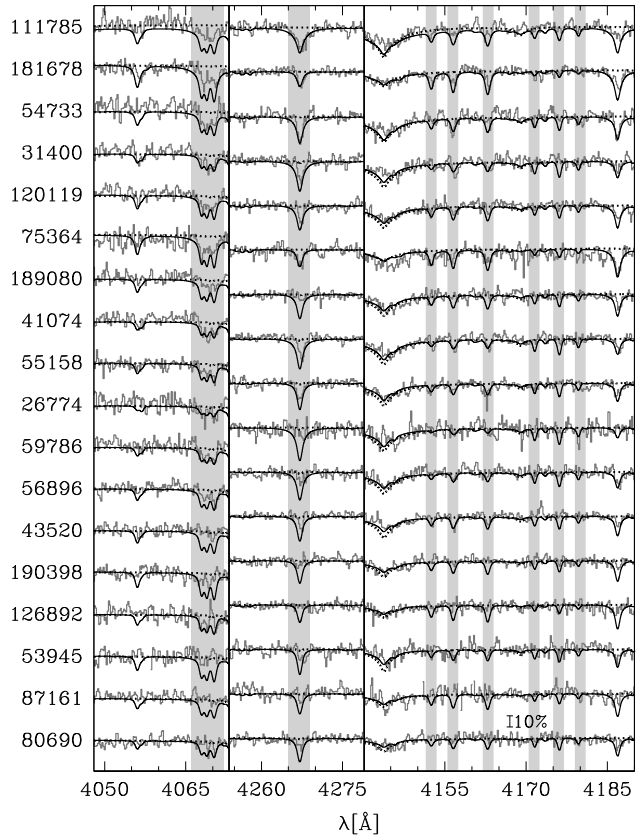

Fig. 8. Spectra of all stars with super-solar helium abundances in spectral regions where strong carbon lines (marked with grey shading) are expected. The helium abundance decreases *from top to bottom* and the stars' names are given. The black solid line marks the model spectrum with a carbon/nitrogen abundance of 3/1% by mass, while the dotted line (horizontal except for the He I line at 4144 Å) indicates the model spectrum with the cluster carbon and nitrogen abundances. We always plot the model spectra that best fit the observed helium and hydrogen lines.

8. Conclusions

From our spectroscopic analysis of the spectra of hot horizontal branch stars, we derive the following conclusions:

1. We have found no evidence of close binaries among our targets.
2. The effective temperatures and surface gravities of the helium-poor HB stars below 20 000 K are at first glance indicative of helium enrichment. The too-low masses derived from these parameters, however, render these results dubious. This, however, does *not* rule out the presence of helium-enriched stars in this temperature range.
3. The parameters of the stars in Group 2 agree well with the predictions of the late hot flasher scenario, if one allows for some residual hydrogen and diffusion effects. Strong arguments in favour of this scenario are the presence of stars with helium abundances in excess of the predictions of D'Antona et al. (2010) and clear evidence of carbon enrichment by at least a factor of 10 in the more helium-rich stars. Additional support is provided by the evolved status of all helium-poor stars above 32 000 K (the hot end of the canonical ZAHB). This does not rule out the possibility that the blue hook stars belong to the helium-enriched sub-population, but this helium enrichment alone cannot explain the observed parameters of the stars (as already stated by Moehler et al. 2007).

Acknowledgements. We thank the staff at the Paranal observatory and at ESO Garching for their excellent work, which made this paper possible. Two of us (GB, AC) were partially supported by Monte dei Paschi di Siena (P.I.: S. Degl'Innocenti) and by PRIN-MIUR2007 (P.I.: G. Piotto). This research has made use of NASA's Astrophysics Data System. We thank the anonymous referee for helpful comments.

References

Bedin, L. R., Piotto, G., Anderson, J., et al. 2004, ApJ, 605, L125
Bergeron, P., Saffer, R. A., & Liebert, J. 1992, ApJ, 394, 228
Bragaglia, A., Carretta, E., Gratton, R., et al. 2010, A&A, 519, A60
Brown, T. M., Sweigart, A. V., Lanz, T., Landsman, W. B., & Hubeny, I. 2001, ApJ, 562, 368
Brown, T. M., Sweigart, A. V., Lanz, T., et al. 2010, ApJ, 718, 1332
Busso, G., Cassisi, S., Piotto, G., et al. 2007, A&A, 474, 105
Calamida, A., Stetson, P. B., Bono, G., et al. 2005, ApJ, 634, L69
Caloi, V., & D'Antona, F. 2005, A&A, 435, 987
Caloi, V., & D'Antona, F. 2008, ApJ, 673, 847
Cassisi, S., Schlattl, H., Salaris, M., & Weiss, A. 2003, ApJ, 582, L43
Cassisi, S., Salaris, M., Anderson, J., et al. 2009, ApJ, 702, 1530
Castellani, M., & Castellani, V. 1993, ApJ, 407, 649
Castellani, V., Calamida, A., Bono, G., et al. 2007, ApJ, 663, 1021
Catelan, M., Grundahl, F., Sweigart, A. V., Valcarce, A. A. R., & Cortés, C. 2009, ApJ, 695, L97
D'Antona, F., & Caloi, V. 2008, MNRAS, 390, 693
D'Antona, F., & Ventura, P. 2007, MNRAS, 379, 1431
D'Antona, F., Bellazzini, M., Fusi Pecci, F., et al. 2005, ApJ, 631, 868
D'Antona, F., Caloi, V., & Ventura, P. 2010, MNRAS, 405, 2295
D'Cruz, N. L., Dorman, B., & Rood, R. T. 1996, ApJ, 466, 359
D'Cruz, N. L., O'Connell, R. W., Rood, R. T., et al. 2000, ApJ, 530, 352
Dalessandro, E., Salaris, M., Ferraro, F., et al. 2011, MNRAS, 410, 694
Di Criscienzo, M., D'Antona, F., & Ventura, P. 2010, A&A, 511, A70
Fabbian, D., Recio-Blanco, A., Gratton, R. G., Piotto, G. 2005, A&A, 434, 235
Gratton, R. G., Sneden, C., Carretta, E., & Bragaglia, A. 2000, A&A, 354, 169
Gratton, R. G., Carretta, E., Bragaglia, A., Lucatello, S., & D'Orazi, V. 2010, A&A, 517. 81
Harris, W. E., 1996, AJ, 112, 1487 (version February 2003)
Hubeny, I., & Lanz, T. 1995, ApJ, 439, 875
Kraft, R. P. 1994, PASP, 106, 553
Lanz, T., & Hubeny, I. 2003, ApJS, 146, 417
Lanz, T., & Hubeny, I. 2007, ApJS, 169, 83
Lanz, T., Brown, T. M., Sweigart, A. V., Hubeny, I., & Landsman, W. B. 2004, ApJ, 602, 342
Lee, Y.-W., Joo, S.-J., Han, S.-I., et al. 2005, ApJ, 621, L57
Miller Bertolami, M. M., Althaus, L. G., Unglaub, K., & Weiss, A. 2008, A&A, 491, 253
Moehler, S., Sweigart, A. V., Landsman, W. B., & Heber, U. 2000, A&A, 360, 120
Moehler, S., Sweigart, A. V., Landsman, W. B., & Dreizler, S. 2002, A&A 395, 37
Moehler, S., Landsman, W. B., Sweigart, A. V., & Grundahl, F. 2003, A&A, 405, 135
Moehler, S., Sweigart, A. V., Landsman, W. B., Hammer, N. J., & Dreizler, S. 2004, A&A 415, 313
Moehler, S., Dreizler, S., Lanz, T., et al. 2007, A&A 475, L5
Moni Bidin, C., Moehler, S., Piotto, G., Momany, Y., & Recio-Blanco, A. 2007, A&A, 474, 505
Napiwotzki, R., Green, P. J., & Saffer, R. A. 1999, ApJ, 517, 399
Norris, J. E. 2004, ApJ, 612, L25
Origlia, L., Ferraro, F. R., Bellazzini, M., & Pancino, E. 2003, ApJ, 591, 916
Piotto, G., Zoccali, M., King, I. R., et al. 1999, ApJ, 118, 1727
Piotto, G., Villanova, S., Bedin, L. G., et al. 2005, ApJ, 621, 777
Piotto, G., Bedin L. R., Anderson, J., et al. 2007, ApJ, 661, L53
Portinari, L., Casagrande, L., & Flynn, C. 2010, MNRAS, 406, 1507
Ripepi, V., Clementini, G., Di Criscienzo, M., et al. 2007, ApJ, 667, L61
Rosenberg, A., Recio-Blanco, A., & Garcia-Marin, M. 2004, ApJ, 603, 135
Saffer, R. A., Bergeron, P., Koester, D., & Liebert, J. 1994, ApJ, 432, 351
Salaris, M., Chieffi, A., & Straniero, O. 1993, ApJ, 414, 580
Sandquist, E. L., Gordon, M., Levine, D., & Bolte, M. 2010, AJ, 139, 2374
Sweigart, A. V. 1997, The Third Conference on Faint Blue Stars, ed. A. G. D. Philip, J., Liebert, & R. A. Saffer (Schenectady: L. Davis Press), 3
Unglaub, K. 2005, The 14th European Workshop on White Dwarfs, ed. D. Koester, & S. Moehler (ASP: San Francisco), ASP Conf. Ser., 334, 297
Villanova, S., Piotto, G., King, I. R., et al. 2007, ApJ, 663, 296
Villanova, S., Piotto, G., & Gratton, R. 2009, ApJ, 499, 755
Whitney, J. H., Rood, R. T., O'Connell, R. W., et al. 1998, ApJ, 495, 284
Zacharias, N., Urban, S. E., Zacharias, M. I., et al. 2004, AJ, 127, 3043